Vortex configurations in a Pb/Cu microdot with a 2×2 antidot cluster

T. Puig,* E. Rosseel, L. Van Look, M. J. Van Bael, V. V. Moshchalkov, and Y. Bruynseraede
Laboratorium voor Vaste-Stoffysica en Magnetisme, Katholieke Universiteit Leuven, Celestijnenlaan 200D, B-3001 Leuven, Belgium

R. Jonckheere
Inter-university Micro-Electronics Center, Kapeldreef 75, B-3001 Leuven, Belgium

(Received 12 March 1998)

We present a detailed study of the transport properties of a superconducting Pb/Cu microdot with a 2×2 antidot cluster. The superconducting-normal (S/N) phase boundary, critical currents, and current-voltage characteristics of this structure have been measured. The S/N phase boundary as a function of field B $[T_c(B)]$ reveals an oscillatory structure caused by the limited number of possible vortex configurations that can be realized in these small clusters of pinning centers (antidots). We have analyzed the stability of these configurations and discussed the possible dissipation mechanisms using the critical current $[J_c(B)]$ and voltage-current $[V(I)]$ characteristics data. A comparison of the experimental data of $T_c(B)$ and $J_c(B)$ with calculations in the London limit of the Ginzburg-Landau theory confirms that vortices can indeed be pinned by the antidots forming a cluster and that the ground-state configurations of the vortices are noticeably modified by sending current through the structure. The possibility of generating phase slips as well as motion of the vortices in the 2×2 antidot cluster will also be discussed.
[S0163-1829(98)01833-5]

I. INTRODUCTION

Laterally modulated superconductors have been intensively studied during the past few years (for reviews, see Refs. 1 and 2). The interest towards these materials was stimulated by the advances in the microfabrication techniques that enabled the production of submicron structures with the relevant dimensions of the order of the superconducting coherence length, $\xi(T)$ and penetration depth $\lambda(T)$. These microstructures impose certain constraints on the behavior of the superconducting order parameter by confining the superconducting condensate within the sample's boundaries, including those introduced through lateral nanostructuring. Superconducting wire networks and Josephson junction arrays (JJA's) are some examples of the laterally modulated films, where the applied magnetic field provides a continuously changing length scale that can explore commensurability between the lattice of vortices and the underlying artificially introduced lateral lattice.[3–5]

In networks, fluxoid quantization governs the properties and defines the allowed quantum states. Circular currents (vortices) are induced around the cells forming the structure, thus defining sets of specific vortex configurations.

Recently, a new class of superconducting systems was introduced, consisting of a regular pinning array formed by a lattice of antidots (i.e., submicron holes) made in a type-II superconducting film.[6,7] At temperatures close to T_c superconductors with an antidot lattice behave like weakly coupled wire networks,[8] where vortex depinning dominates the dissipation.[3–5] Well below the transition temperature, where the fluxoid quantization condition implies flux quantization at the antidots, features appear in the magnetization,[6,9] critical currents,[10] and S/N phase boundaries[7] that have been attributed to the formation of multiquanta vortices at the antidots.

Taking into account the vortex-vortex interactions in samples with $\sim10^6$ antidots is, however, not a simple exercise due to the very large number of the interacting vortices. From this point of view, *a microdot with an antidot cluster* (2×2, 3×3, etc.) with a small number of interacting vortices is a very promising ''intermediate'' system between a single superconducting loop with a finite strip width and a superconducting film with a huge array of antidots. At the same time, using finite microdots with four antidots (the antidot cluster), we still keep the most essential features of the vortex-vortex interactions in the presence of antidots. The reduced number of interacting vortices simplifies exact calculations that can also be extrapolated for the analysis of the vortex behavior in substantially larger antidot arrays.

In this paper, we study the transport properties of such a model superconducting microsquare containing four antidots. Further on, for simplicity, we shall call this structure a ''2×2 antidot cluster.'' This system can be considered as four unit cells of the regular square lattice of antidots and the initial simplicity makes the 2×2 antidot cluster a good candidate for achieving an insight into the stable vortex configurations expected for larger systems. Only a very limited number of vortex configurations are allowed for the 2×2 antidot cluster, and therefore both the experimental results are less difficult to be interpreted and a computational analysis is also easier to perform. Additionally, the limited number of vortex configurations also makes these structures interesting for flux logic applications.[11]

In this paper, we focus on measurements of the superconducting/normal (S/N) phase boundary, the magnetoresistance, the critical currents, and the $V(I)$ characteristics of a superconducting microsquare with four antidots. These experimental results have been compared with calculations in the London limit of the Ginzburg-Landau theory and in

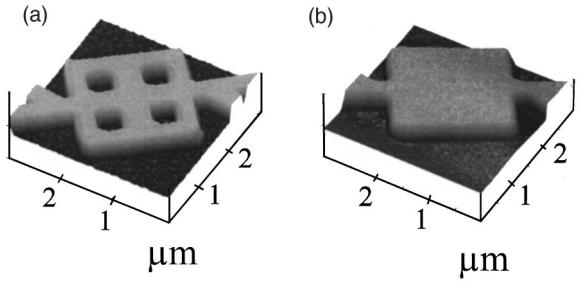

FIG. 1. Atomic force microscopy picture of (a) the 2×2 antidot cluster and (b) the reference sample without antidots.

the framework of the de Gennes-Alexander model.[12] The comparison has demonstrated that several well-defined vortex configurations can be induced in these samples by properly tuning the magnetic field and the temperature. At very low transport currents, only four of these configurations are stable. By increasing the transport current, however, other flux phases, which are unstable without transport current, can be realized. Based on the $V(I)$ characteristics data, we also consider how the occupation of antidots by vortices influences the onset of dissipation.

The paper is organized as follows. Section II describes the sample preparation, the experimental techniques, and characteristic superconducting parameters of the Pb/Cu 2×2 antidot cluster. In Sec. III A, we present the results on the S/N phase boundary $T_c(B)$ for the 2×2 antidot cluster and a reference superconducting microsquare without antidots. The calculation of the S/N phase boundary for the 2×2 antidot cluster in the London limit and in the framework of the de Gennes-Alexander model[12] is described and compared with the experimental data. The discussion of possible effects of disorder is also presented. Section III B comprises the experimental results of the critical currents and $V(I)$ characteristics. The $V(I)$ data are used to determine the dissipation related to the vortex motion in the 2×2 antidot cluster.

II. EXPERIMENT

A. Sample preparation and characterization

The 2×2 antidot clusters consisting of microsquares of 2×2 μm^2 with four antidots (i.e., submicron holes of 0.53×0.53 μm^2 and center-to-center distance of 1 μm) were written by e-beam lithography in positive polymethylmetacrylate (PMMA) resist onto SiO_2 substrates. Afterwards, a bilayer consisting of 50-nm-thick Pb and 17-nm-thick Cu was evaporated in one single run in a molecular-beam epitaxy apparatus at pressures of 5×10^{-8} Torr. The SiO_2 substrates were N_2 cooled during evaporation, which decreased the film roughness down to 1.4 nm and suppressed the interdiffusion at the Pb/Cu interface.[13] After the lift-off processing, the samples were characterized by x-ray, atomic force microscopy (AFM), and scanning electron microscopy. The x-ray results show that the Pb/Cu bilayers are polycrystalline with a preferential growth of the Pb and Cu in the (111) direction. An AFM picture of the 2×2 antidot cluster of Pb/Cu with four leads attached for electrical connection is shown in Fig. 1(a). Also shown [Fig. 1(b)] is the AFM image of a reference sample that consists of a Pb(50 nm)/Cu(17 nm) microsquare of 2×2 μm^2 without antidots.

The top Cu layer of 17 nm, evaporated onto the Pb film, was used to protect the Pb film from oxidation and to enable electrical connection to the experimental apparatus using a wire bonding technique through the 150×150 μm^2 electrical pads of the sample. Besides that, the Cu layer also changes the coherence length and the penetration depth of the Pb layer. We discuss the influence of this Cu layer on the superconducting properties of the Pb/Cu bilayers in terms of proximity induced superconductivity in the next section.

The electrical transport properties were measured in a ^{3}He cryostat using the four-probe technique. The magnetic field was applied perpendicular to the film surface and the temperature stabilization was better than 0.4 mK. Since the mesoscopic samples are very sensitive and easily destroyed by electrostatic charges, all necessary grounding precautions were taken and 1.2 kΩ resistors were connected in series with each lead to damp parasitic voltage peaks. The resistance measurements were performed using an ac-resistance bridge whereas the $V(I)$ characteristics and critical current measurements were carried out using a dc power supply and a nanovoltmeter. The S/N phase boundary was determined automatically by keeping the sample resistance at a specific fixed value (usually at 10% of the normal-state resistance) and varying the magnetic field and temperature. Similarly, the critical current measurements as function of field were performed by keeping the sample at a certain fixed voltage and varying the applied current and magnetic field.

B. Superconducting parameters of the Pb/Cu bilayer

In order to study the Pb(50 nm)/Cu(17 nm) bilayer that was used for the 2×2 antidot clusters, we also prepared a single Pb(50 nm) and Cu(17 nm) film and measured their properties. Below, we present the summary of these results.

Comparing the resistivity due to electron-phonon scattering, for the Pb(50 nm) film, $\rho_{300\ K}-\rho_{7\ K}=27.8$ $\mu\Omega$ cm and for the 17 nm Cu thin films $\rho_{300\ K}-\rho_{7\ K}=12.47$ $\mu\Omega$ cm, with the published bulk values of 21 $\mu\Omega$ cm and 1.7 $\mu\Omega$ cm, respectively,[14] we conclude that the resistivity of the Pb film approaches the bulk value whereas the resistivity of the Cu film is enhanced with respect to the bulk value due to the finite-size effect.[15] The mean-free paths at 7 K determined from the resistivity values are $l_{Pb}=33$ nm and $l_{Cu}=7.2$ nm, respectively. Thus, both single films, Pb (50 nm) and Cu (17 nm), are in the dirty limit since $l_{Pb}<\xi_0$ and $\lambda_{Cu}\gg1$,[16] respectively, where $\xi_0=83$ nm is the BCS coherence length of the Pb (Ref. 17) and $\lambda_{Cu}=(\hbar v_F)/(2\pi T l_{Cu} k_B)=38$ at 7 K is a dimensionless impurity parameter.

The superconducting properties of the S layer are characterized by two important lengths, the temperature-dependent coherence length, $\xi_S(T)=0.85\sqrt{\xi_0 l_{Pb}}/\sqrt{1-T/T_c}$, and the penetration depth, $\lambda_S(T)=0.66\lambda_L\sqrt{\xi_0/l_{Pb}}/\sqrt{1-T/T_c}$, in the dirty limit. Here λ_L is the London penetration depth.[17] For the Pb (50 nm) film at $T=0$ K, these two quantities take the values $\xi_{Pb}(0)=45$ nm and $\lambda_{Pb}(0)=39$ nm, respectively. Experimentally, we can also determine $\xi_{Pb}(0)$ from the re-

lation between the perpendicular second critical field $B_{c2,S}$ in a S layer and its in-plane superconducting coherence length $\xi_S(0)$ given by

$$B_{c2,S}(0)=\frac{\Phi_0}{2\pi\xi_S(0)^2}, \tag{2.1}$$

where $\Phi_0=h/2e$ is the flux quantum. The coherence length obtained in this way is $\xi_{Pb}(0)=36$ nm. Now, we can determine the Ginzburg-Landau parameter $\kappa_{Pb}=\lambda_{Pb}(0)/\xi_{Pb}(0)=1.08$, and since $\kappa_{Pb}>0.7$, we conclude that the single Pb layer is a type-II superconductor.

By covering the Pb with a Cu layer, a superconducting Pb/Cu bilayer is obtained with different characteristic parameters than those of the single Pb film. We therefore define the effective superconducting parameters as the ones that can be determined from measurements on a Pb/Cu bilayer.

The Pb/Cu antidot clusters had a superconducting transition temperature, $T_{c_{NS}}=6.05$ K, whereas the reference sample (i.e., square of $2\times2\ \mu\mathrm{m}^2$ without antidots) had a $T_{c_{NS}}=5.55$ K. The systematic difference in critical temperature between the perforated and reference sample is probably related to a difference of the electrical properties of the interface between the Pb and Cu layers. The possibility for an oxidation at the Pb/Cu interface is higher in perforated samples. This results in a smaller proximity coupling and, possibly, a higher effective critical temperature. Nevertheless, it is obvious that in both cases the top Cu layer decreases $T_{c_{NS}}$ below the $T_c=7.2$ K of the bulk Pb due to the proximity effect.[18]

From the measured critical fields of the Pb(50 nm)/Cu(17 nm) bilayer, we determined an effective superconducting coherence length as $\xi_{Pb/Cu}(0)=39$ nm, using Eq. (2.1).

One may expect that an effective penetration depth for the (NS) bilayer $\lambda_{NS}(0)$ could also be defined. Especially, since there should exist a penetration depth $\lambda_N(0)$, determining the decay of the magnetic field in the normal layer with proximity coupling, which should be different from $\lambda_S(0)$. The exact definition of these two quantities, $\lambda_N(0)$ and $\lambda_{NS}(0)$, is not obvious. Since we know that $\lambda_{NS}(0)>\lambda_S(0)$, we will estimate a lower limit for $\lambda_{NS}(0)$ as $\lambda_{Pb}(0)=39$ nm. Further in the paper (see Sec. III B 2), a more accurate estimate for $\lambda_{NS}(0)$ will be given.

With this information, we can determine a lower limit for the effective Ginzburg-Landau parameter $\kappa_{Pb/Cu}=\lambda_{Pb/Cu}(0)/\xi_{Pb/Cu}(0)$ as 1 for the Pb(50 nm)/Cu(17 nm) bilayer. Since $\kappa_{Pb/Cu}>0.7$, the Pb/Cu bilayer is a type-II superconductor. As shown above, by covering Pb with a thin Cu layer, we are not only protecting the former against oxidation, but we are also changing, in certain limits, the effective ξ and λ.

Pb/Cu bilayers are good candidates for studying proximity coupling effects[19] between a superconductor (S) and a normal metal (N) since interdiffusion hardly exists at the interface of these materials, especially when they are evaporated at low temperature. Therefore, each material remains within its own boundaries.

The proximity effect[18] refers to the induction of superconductivity in a contacting normal metal by the decay of the superconducting order parameter Δ from a superconductor into a normal metal. Not only the order parameter in the superconductor decays when approaching the S/N interface from the superconducting size, but also a nonvanishing superconducting order parameter nucleates in the N layer close to the interface. Thus, one of the most important parameters defining the proximity effect between two layers is the so-called coherence length of the normal layer ξ_N, which determines the length in the normal metal over which Cooper pairs can diffuse (see Fig. 2). In the dirty limit and for our Cu parameters, $\xi_{Cu}=(\hbar v_F l_{Cu}/6\pi k_B T)^{1/2}=28$ nm at 6 K, where v_F is the Fermi velocity of Cu. Note that $\xi_{Cu}>d_{Cu}$ where $d_{Cu}=17$ nm is the Cu thickness, which means that the superconducting order parameter is finite over the full thickness of the Cu layer in the temperature interval at which experiments on the Pb/Cu antidot cluster were performed ($5\ \mathrm{K}<T<6\ \mathrm{K}$).

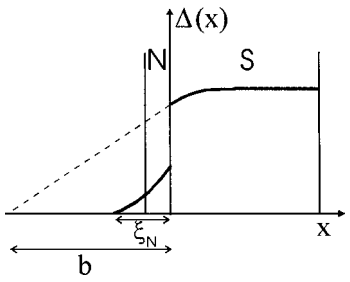

FIG. 2. Schematic representation of the spatial dependence of the superconducting order parameter at the interface between the superconductor (S) and the normal material (N) of the Pb/Cu bilayers studied in this paper. The two characteristic parameters for proximity induced superconductivity, i.e., the coherence length in the normal layer ξ_N and the extrapolation length b are indicated.

Another very interesting parameter in proximity induced superconductivity is the extrapolation length,[19] $b=\gamma\xi_{Cu}(T)\coth(d_{Cu}/\xi(T)=98$ nm at 6 K in the dirty limit (see Fig. 2), where $\gamma=\rho_{Cu}/\rho_{Pb}$. This parameter b is a measure of the unfavorable influence of the N layer on the superconductivity of the S layer. If $b\ll\xi_S(T)$, the effects of proximity coupling are important, whereas if $b\gg\xi_S(T)$, the superconducting order parameter at the interface is almost not changed and the effects of proximity coupling are negligible. In our case at 6 K, $b=98$ nm, $\xi_{Pb}(6K)=108$ nm, thus the proximity effect has an intermediate strength in the Pb(50 nm)/Cu(17 nm) bilayer.

We can classify our samples as being in the Cooper limit[19] since they fulfill the constraints $d_{Cu}<\xi_{Cu}$ and $d_{Pb}<\xi_0$. In this limit, $\Delta(x)$ can be taken as a constant over the individual layers and discontinuous at the interface. The perpendicular second critical field $B_{c2,NS}$, for a (NS) bilayer of thickness (d_N+d_S), can then be determined from the second critical field of the single superconducting layer $B_{c2,S}$ by the dirty limit expression.[16]

$$B_{c2,NS}(0)=\frac{B_{c2,S}(0)}{1+\eta d_N/d_S}, \tag{2.2}$$

where $\eta=\rho_S/\rho_N$ for a specular scattering at the interface. This expression is in good agreement with our experimental results on bilayers with different Cu thicknesses. In particular, for the bilayer Pb(50 nm)/Cu(17 nm) used for the fabrication of the antidot cluster, Eq. (2.2) reduces to $B_{c2,NS}(0)$

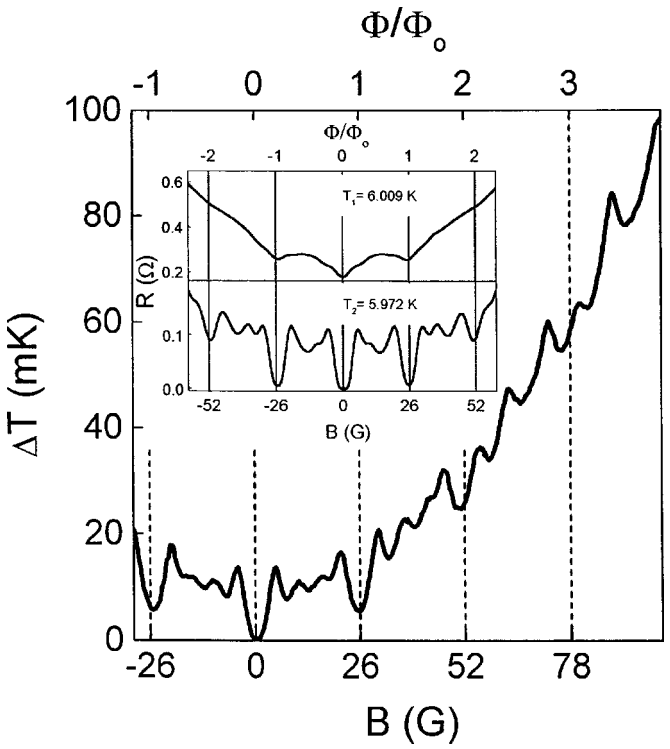

FIG. 3. Experimental S/N phase boundary of the 2×2 antidot cluster determined with a criterium of 10% of the normal-state resistance. Two typical magnetoresistance curves are shown in the inset. The ac measuring current was 1 μA.

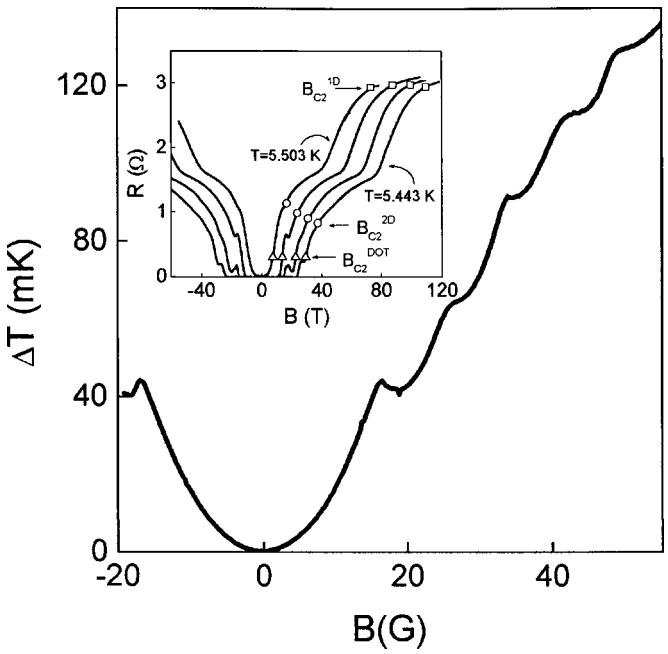

FIG. 4. Experimental S/N phase boundary of the reference sample determined with a criterium of 10% of the normal-state resistance. The inset shows four magnetoresistance curves measured at $T=5.503$, 5.482, 5.462, and 5.443 K. The ac measuring current was 1 μA. The second critical magnetic fields for the 1D transition (B_{c2}^{1D}), the 2D transition (B_{C2}^{2D}), and the transition of the microsquare (B_{c2}^{DOT}) are shown.

$=\alpha B_{c2,S}(0)$ with $\alpha=0.91$. Experimentally, we have obtained $\alpha=0.86$, which is in agreement with the calculated value within 5%. Taking into account that the scattering at the interface is probably not completely specular, the obtained agreement is quite good.

Combining Eqs. (2.1) and (2.2), one can obtain the ratio between the superconducting coherence length for the Pb(50 nm) layer and that of the Pb(50 nm)/Cu(17 nm) bilayer, $\xi_{Pb/Cu}(0)/\xi_{Pb}(0)=1.05$. Using the value $\xi_S(0)=36$ nm for the Pb(50 nm) film, we expect, according to this relation, that $\xi_{Pb/Cu}=1.05\xi_S(0)=38$ nm for the Pb(50 nm)/Cu(17 nm) bilayer film, which is within 5% agreement with the ''experimental'' value determined from the measured second critical fields of bilayers of that specific thickness, $\xi_{Pb/Cu}(0)=39$ nm.

In summary, from the analysis of the superconducting properties of the Pb/Cu bilayer we can conclude that (i) the Pb(50 nm)/Cu(17 nm) bilayer shows proximity induced superconductivity of an intermediate strength; (ii) the proximity induced superconductivity penetrates through the whole thickness of the Cu layer; and (iii) the effective parameters $B_{c2,NS}(0)$, $\xi_{NS}(0)$, and $\lambda_{NS}(0)$ for the bilayer films have been determined from the experimental results.

III. RESULTS AND DISCUSSION

A. The S/N phase boundary

1. Experimental results

Figure 3 shows the (S/N) phase boundary $\Delta T_c(B)=T_c(0)-T_c(B)$ of the Pb(50 nm)/Cu(17 nm) 2×2 antidot cluster measured with the criterium of 10% of the normal-state resistance. Pronounced periodic oscillations of $T_c(B)$ are observed every 26 G. Defining a flux quantum per antidot as $\Phi_0=h/2e=B\cdot S$, where S is an effective area per antidot ($S=0.8$ μm^2), the oscillations with periodicity of 26 G can be correlated with a magnetic flux per antidot, $\Phi=n\Phi_0$, where n is an integer number. In each of these 26 G periods, smaller dips appear at approximately 7.5, 13, and 18 G. The smaller dips correspond to approximately $\Phi/\Phi_0=0.3$, 0.5, and 0.7.

Superimposed with these oscillations, a parabolic background is observed, reflecting the $B(T)$ dependence of the second critical field of the quasi-one-dimensional stripes constituting the antidot cluster, $B_{c2}^{1D}=(\sqrt{12}\Phi_0)/[2\pi w\xi(T)]$ (Ref. 20) where w is the width of the stripe. From this formula, an effective coherence length $\xi_{NS}(0)=35$ nm is obtained for this particular sample with $T_c=6.05$ K. Above 52 G, deviations from the main 26 G periodicity and intermediate substructure are observed.

In the inset of Fig. 3, two magnetoresistance curves, $R(B)$, measured at $T_1=6.009$ K and $T_2=5.972$ K, are shown. At T_1 only minima at $n\times26$ G are distinctly observed. At T_2 an additional substructure appears in each period. The magnetoresistance results confirm the features observed in $T_c(B)$. A cut of the $T_c(B)$ boundary at high temperature (i.e., $T\sim T_1$) reveals only the main 26 G oscillations, whereas a cut at lower temperatures results in the full substructure.

Figure 4 shows the (S/N) phase boundary, $\Delta T_c(B)=T_c(0)-T_c(B)$, of the reference sample (i.e., a superconducting microsquare without antidots [see Fig. 1(b)] measured at

10% of the normal-state resistance. In this case, oscillations are also observed, however they are clearly different from those presented in Fig. 3. The first oscillation of $\Delta B_1 \sim 16$ G is followed by quasiperiodic oscillations with decreasing ΔB ($\Delta B_2 = 9.9$ G, $\Delta B_3 = 8.2$ G, $\Delta B_4 = 7.5$ G, $\Delta B = 7.1$ G). In addition, the superimposed background of Fig. 4 follows a linear relation instead of the parabolic dependence seen in Fig. 3. The oscillations are caused by the confinement of the superconducting condensate in the dot as revealed by other studies.[21,22] The remark must be made that the first two periods are noticeably larger than those predicted in Ref. 22. The other periods correspond to the calculations within 15%. The linear background observed in Fig. 4 is related to the second critical field of a two-dimensional (2D) system B_{c2}^{2D}, given by the expression $B_{c2}^{2D} = \Phi_0/2\pi\xi(T)^2$. From this linear background an effective coherence length, $\xi_{NS}(0) = 41$ nm, is determined for this specific sample with $T_c = 5.55$ K.

In the inset of Fig. 4, the magnetoresistance curves for the reference sample are shown at four different temperatures. For any of these $R(B)$ curves, two large drops of resistance are observed when decreasing the magnetic field. In addition, for each curve and at low fields, one single small dip appears. This dip shifts to higher magnetic fields when decreasing the temperature and is responsible for the oscillations observed in $T_c(B)$. On the contrary, the two drops of resistance may be explained by the influence of the four narrow superconducting leads that are attached to the microsquare (two for sending the transport current and two to measure the voltage). These leads are quasi-one-dimensional wires and therefore they become superconducting below the field $B_{c2}^{1D} = (\sqrt{12}\Phi_0)/2\pi w\xi(T)$. However, the dot itself has a second critical field transition given by $B_{c2}^{2D} = \Phi_0/[2\pi\xi(T)^2]$, as mentioned above.

Taking into account that the transition to the superconducting state takes place at higher magnetic fields for the 1D system (i.e., leads) than for the 2D system (i.e., microsquare), one expects to attain the following situation: When decreasing the magnetic field, starting from the normal state, a first resistive drop is observed, caused by a transition to the superconducting state of the narrow current and voltage leads. The fact that the resistance of the microsquare is affected by this transition, does not mean that the ''four-point'' resistance measurement contains a portion of the leads, but arises from those parts of the cluster that become superconducting due to their proximity to the leads. The theoretical critical field values for the leads, as calculated from the above formula for B_{c2}^{1D} using the effective coherence length ξ_{NS} obtained from the linear background of $T_c(B)$, are marked by the open squares in the inset of Fig. 4. The first resistance drop of the dot takes place at slightly lower fields than the N/S transition of the leads, since they are only in proximity coupling with the dot. Therefore, the squares indicating B_{c2}^{1D} fall on a horizontal straight line above the onset of the resistance drop, and not in the middle of the transition.

Further decreasing the magnetic field, we cross the line B_{c2}^{2D} at which the microsquare becomes superconducting and a second resistance drop is initiated (see the open circles in the inset of Fig. 4). In this part of the curve, small dips appear in the magnetoresistance due to the dot geometry. These dips are responsible for the oscillations observed in the $T_c(B)$ curve. Similar two-step $R(B)$ transitions have been observed by Chi *et al.*,[23] who studied narrow 1D superconducting wires connected to large 2D contact pads. In their case, the proximity coupling between the 1D wires with a large critical field and the 2D pads with a small critical field gave rise to a two-step behavior comparable to our results.

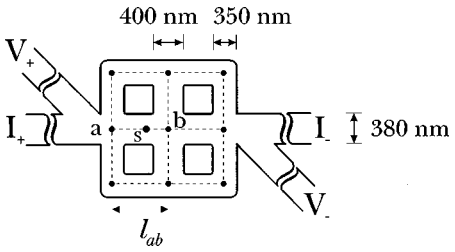

FIG. 5. Schematic representation of the 2×2 antidot cluster with average dimensions indicated. The network approximation used in the one-dimensional model is drawn with a dashed line. The dots denote the nine nodes considered in the model.

We have to note that the expression used to calculate the B_{c2}^{2D} values corresponds only to the linear $T_c(B)$ background; the periodic oscillations superimposed with it are not considered in this expression and, thus, it is not surprising that the calculated values for B_{c2}^{2D} (see the open circles in the inset of Fig. 4) do not lie on one horizontal line. However, if we determine the critical magnetic field values from the measurements of $T_c(B)$ (see Fig. 4) where both the background and oscillations due to the dot geometry are considered at a criterium of 10%, we obtain the open triangles shown in the inset. Their position agrees with all the expectations, i.e., the triangles lie on a horizontal line which is at 10% of the normal-state resistance.

2. Calculations of the $T_c(B)$ phase boundary

In order to calculate the S/N phase boundary of the 2×2 antidot cluster, we have approximated the cluster geometry by a square network of quasi-one-dimensional superconducting wires with a width w and a length l (see Fig. 5). Adjacent nodes (i,j) are coupled by a supercurrent depending on the gauge-invariant phase difference γ_{ij} between the nodes

$$\gamma_{ij} = \phi_j - \phi_i + \frac{2\pi}{\Phi_0}\int_i^j \mathbf{A}\cdot d\mathbf{l}, \tag{3.1}$$

where ϕ_i is the phase of the superconducting order parameter at site i, $\Phi_0 = h/2e$ is the flux quantum, $\mathbf{A}$ is the magnetic vector potential, and $d\mathbf{l}$ is a segment along the wire. First of all, we have used the approximation developed for weakly coupled wire networks,[3,5,24,11] the ''interacting loop-current (ILC) model,'' which neglects the variation of the order parameter along the superconducting wires of the network and only considers the phase variations. This simplification is therefore equivalent to the London limit of the Ginzburg-Landau theory, and leads to a linear current-phase relation

$$I_{ij}=\frac{\Phi_0 wd}{2\pi\mu_0\lambda^2 l}\gamma_{ij}=I_0\gamma_{ij}, \tag{3.2}$$

where I_{ij} is the supercurrent from i to j, d is the wire thickness, and λ is the superconducting penetration depth of the material. The resulting kinetic energy for each wire (i,j) can be expressed as

$$E_{ij}=\frac{\Phi_0^2 wd}{4\pi^2\mu_0\lambda^2 l}\gamma_{ij}^2 \tag{3.3}$$

and is a quadratic function of phase differences. The prefactor in Eq. (3.3) defines the coupling strength between the adjacent nodes and is denoted as

$$E_J\equiv\frac{\Phi_0^2 wd}{4\pi^2\mu_0\lambda^2 l}=\frac{\hbar}{2e}I_0. \tag{3.4}$$

To obtain the possible energy states of the cluster, all phase differences γ_{ij} have to be determined. This is done by imposing current conservation at each node

$$\sum_j I_{ij}=I_i^{ext}, \tag{3.5}$$

where I_i^{ext} is the transport current fed into node (i), and by applying the fluxoid quantization condition to each individual loop,

$$\sum_{(i,j)}\gamma_{ij}=2\pi\left(n_k-\frac{\Phi}{\Phi_0}\right), \tag{3.6}$$

where the sum is taken over the wires of the kth cell, n_k $(k=1,...,4)$ is the flux quantum number of the kth cell, and Φ is the magnetic flux. An estimation of the self-inductance for an individual cell of the antidot cluster gives $\mathcal{L}\approx 2$ pH. Since most of the results are obtained close to T_c, the flux generated by the circulating currents is negligibly small. As a consequence we have not taken the self- and mutual-inductance effects into account in our theoretical analysis and Φ is considered to be equal to the external magnetic flux. By solving Eqs. (3.5) and (3.6) for the γ_{ij}'s at a given magnetic field and summing the corresponding energies E_{ij} over all branches (i,j) of the system, we obtain the total kinetic energy of the 2×2 antidot cluster:

$$E=\frac{1}{2}\sum_{(i,j)}E_J\gamma_{ij}^2. \tag{3.7}$$

Since the phase differences are found from Eqs. (3.5) and (3.6), the total energy E for each set of quantum numbers n_k $(k=1,\ldots,4)$ becomes dependent on the magnetic flux through the cells. In Fig. 6(a) the total energy E is plotted as a function of the magnetic flux for the case of $I_i^{ext}=0$ and for all wires with identical lengths and widths. We have omitted the parabolic contribution arising from the finite width of the wires. Since the energy is periodic in Φ with a period Φ_0, we have only plotted the first period. Each set of n_k $(k=1,...,4)$ values corresponds to a different vortex configuration and gives rise to an energy branch that is quadratic with the magnetic flux. Due to the symmetry of the structure, most of the branches are degenerate and only six principal parabolas can be distinguished. The S/N phase boundary is given by the branch that has the lowest energy for a given value of the flux[17]

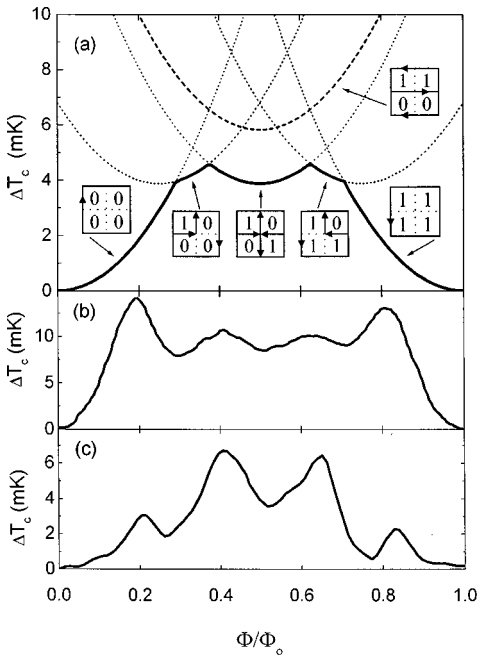

FIG. 6. (a) Theoretical phase boundary $\Delta T(\Phi/\Phi_0)$ obtained in the London limit of the Ginzburg-Landau theory (solid line). The total energy for the six vortex configurations is shown by a dotted line. The dashed line indicates the nonstable ''parallel vortex configuration.'' The schematic representation of the vortex states in each parabolic branch is also sketched by means of the corresponding n_k quantum numbers. (b) First period of the experimental phase boundary shown in Fig. 3 after subtraction of the parabolic background ($I_{ac}=1\ \mu$A). (c) same as (b) but for $I_{ac}=3\ \mu$A.

$$\Delta T_c(\Phi)=\frac{8\pi^2\mu_0\lambda^2\xi(0)^2 T_c}{\Phi_0^2 V}\min_{n_1,\ldots,n_4}(E), \tag{3.8}$$

where V is the total volume of the structure, T_c is the critical temperature at zero field, and $\xi(0)$ is the coherence length at $T=0$. The phase boundary is therefore composed of five branches and has three minima at $\Phi/\Phi_0=0$, 0.5, 1 and four cusps at $\Phi/\Phi_0=0.3$, 0.37, 0.63, 0.7 [see Fig. 6(a)]. At the first branch, around $\Phi=0$, all the $n_k=0$ $(k=1,...,4)$ and a screening current is present only at the edge of the structure. When Φ increases, the fourfold degenerate state with one vortex at one of the cells becomes more stable. The transition occurs at $\Phi/\Phi_0=0.3$. At $\Phi/\Phi_0=0.37$, a doubly degenerate diagonal state becomes favorable, where two vortices occupy one of the diagonals of the cell. Note that this state (which is the analog of the ''checkerboard'' vortex configuration in antidot lattices[25]) has a lower energy than the configuration where two adjacent cells are occupied by vortices (parallel state). The diagonal state could be of interest for flux quantum logic applications.[11] In higher fields, a third vortex enters the cluster at $\Phi/\Phi_0=0.7$ and finally around $\Phi/\Phi_0=1$ all the cells are filled and only an edge current is flowing, now counterclockwise.

It is interesting to note that Eqs. (3.2)–(3.7) are similar to the equations describing the supercurrent and the energy in

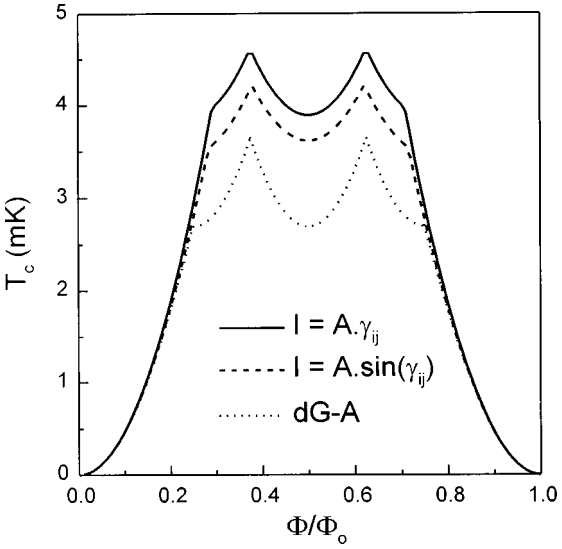

FIG. 7. Comparison of the theoretical phase boundaries obtained for the London (dashed line), Josephson junction array (solid line), and de Gennes-Alexander (dotted line) approaches.

Josephson-junction arrays.[3] In JJA's however, the current-phase relation is sinusoidal and only the phase differences over the Josephson junctions have to be considered. It turns out that the differences between the linear and the ''JJA'' models are not very important when the static properties in a magnetic field are considered. For comparison, we show in Fig. 7 the $E(\Phi)$ curve for a JJA together with the one obtained for the linear relation. Nearly identical energy branches are indeed found, caused by the obvious fact that the sinusoidal current-phase relation can be approximated by a linear one for small phase differences.

For completeness, we also show in Fig. 7 the curve predicted by the linearized de Gennes-Alexander[12] formalism for strong-coupling one-dimensional wire networks, which incorporates phase and amplitude variations of the order parameter along the wires of the network. This formalism assumes that the diameter of the superconducting strands that constitute the network is smaller than both the coherence length and penetration depth. In that way, the problem becomes 1D, and the order parameter Ψ_s at a position s on a wire connecting two adjacent nodes a and b (see Fig. 5) can be expressed as follows:

$$\Psi_s=\frac{e^{i\gamma_{as}}}{\sin\left(\frac{l_{ab}}{\xi(T)}\right)}\left[\Psi_a\sin\left(\frac{l_{ab}-l_{as}}{\xi(T)}\right)+\Psi_b e^{-i\gamma_{ab}}\sin\left(\frac{l_{as}}{\xi(T)}\right)\right], \tag{3.9}$$

where Ψ_a and Ψ_b are the order parameters at the nodes a and b, l_{ab} is the distance between points a and b, and γ_{ab} is the line integral of the vector potential multiplied by $2\pi/\Phi_0$. From the second Ginzburg-Landau equation it is possible to determine the supercurrent density through the branch. It depends sinusoidally on the phase difference between the nodes a and b, similar to the current through a Josephson junction

$$J_{ab}=\frac{2e\hbar}{m^*\xi(T)}|\Psi_a||\Psi_b|\frac{\sin(\phi_a-\phi_b-\gamma_{ab})}{\sin\left(\frac{l_{ab}}{\xi(T)}\right)}. \tag{3.10}$$

Applying the standard boundary conditions at a node a gives rise to the Alexander node equations

$$\sum_n\left[-\Psi_a\cot\left(\frac{l_{an}}{\xi(T)}\right)+\Psi_n\frac{e^{-i\gamma_{an}}}{\sin\left(\frac{l_{an}}{\xi(T)}\right)}\right]=0, \tag{3.11}$$

which express the current conservation at node a similar to Kirchhoff's current law for resistor networks. The sum is taken over all nodes n that are nearest neighbors of node a (see Fig. 5). If this equation is written for all nodes in the network, this leads to a characteristic determinant that must be zero for the existence of a nontrivial solution. We obtain

$$\begin{aligned}&\left(1+2\cos\frac{2\pi\Phi}{\Phi_0}-3\cos\frac{2l_{ab}}{\xi(T)}\right)\\&\times\left(1+2\cos\frac{2\pi\Phi}{\Phi_0}+3\cos\frac{2l_{ab}}{\xi(T)}\right)\\&\times\left(1+3\cos\frac{2l_{ab}}{\xi(T)}-2\sin\frac{2\pi\Phi}{\Phi_0}\right)\\&\times\left(1+3\cos\frac{2l_{ab}}{\xi(T)}+2\sin\frac{2\pi\Phi}{\Phi_0}\right)=0,\end{aligned} \tag{3.12}$$

where Φ is the flux of the applied magnetic field per antidot. Equating the first factor to zero, one obtains a curve defining the first and the fifth branch of the $T_c(B)$ phase boundary. Likewise, the middle three branches are determined by the other three factors (see Fig. 7).

This linearized approach is valid only close to T_c. At lower temperatures, the nonlinear version of this model should be applied.[26,27]

The qualitative agreement between the ILC model [see Fig. 6(a)] and the experimental curves of Figs. 6(b) and 6(c), where the parabolic background has been subtracted, is fairly good. The measurement of curve (b) was performed with an ac current of 1 μA, the one in (c) with 3 μA. The five parabolas corresponding to the different states are found back in the experimental plots. An important difference is, however, that two maxima appear in the experimental phase boundaries at $\Phi/\Phi_0\simeq 0.2$ and 0.8 that are not reproduced in the calculations. The $\Delta T_c(\Phi)$ dependence for the states with all $n_k=0$, or all $n_k=1$, thus seems steeper than predicted by the theoretical model and it also has a larger amplitude. Strangely, the agreement with the theoretical curve, which is calculated for zero transport current, is better in curve (c), where the highest transport current was used. In addition, the experimental $\Delta T_c(\Phi)$ (see Fig. 3) shows a considerable parabolic background, some distortions, and a disappearance of the substructure above $2\Phi_0$.

As was mentioned previously, the parabolic background (''diamagnetic shift'') is due to the penetration of the magnetic field in the volume of the wires[2,20] and can be taken into account by adding the term

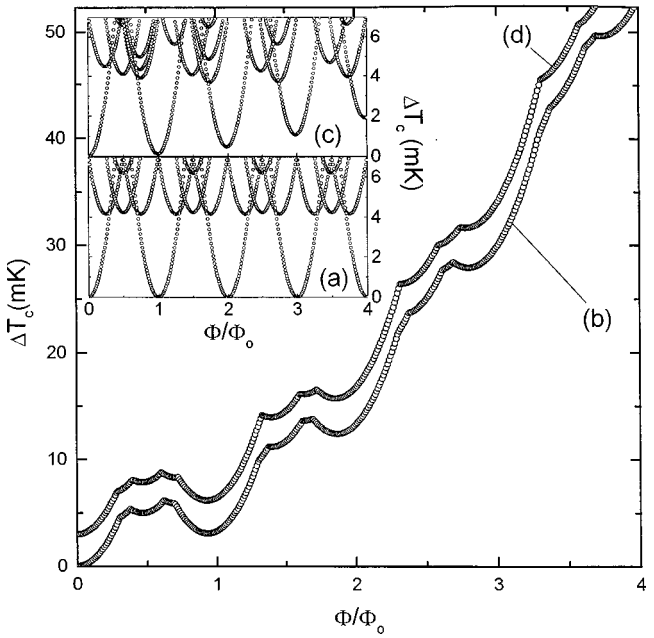

FIG. 8. (a) Theoretical phase boundary for an ideal one-dimensional antidot cluster. (b) Theoretical phase boundary for an antidot cluster considering the effects coming from the magnetic field penetration in the quasi-one-dimensional wires. (c) Theoretical phase boundary for an antidot cluster taking into account the effects induced by areal disorder. (d) Theoretical phase boundary where the contributions shown in (b) and (c) are both considered.

$$\frac{1}{2}\sum_{(i,j)} E_J \frac{\pi^2 B^2 l^2 w^2}{12\Phi_0^2} \tag{3.13}$$

to the right-hand side of Eq. (3.7). The effect of this background is shown in Fig. 8. Curve (a) shows $\Delta T_c(\Phi)$ obtained from Eqs. (3.7) and (3.8) for the antidot cluster. Curve (b) considers the case of a finite linewidth [Eq. (3.13)] with $w=0.35$ μm for wires at the edges of the network and $w=0.4$ μm for the wires connecting the edges with the central node (see Fig. 5). Note in curve (b) that as the field is increased, the ΔT_c amplitude due to fluxoid quantization in the structure becomes quite small with respect to the shift caused by the background, and the amplitude of the oscillations gradually decreases.

After discussing in detail the first period of the phase boundary $T_c(\Phi/\Phi_0)$, we would like to analyze briefly the possible reasons for the shift of the $T_c(\Phi/\Phi_0)$ minima in the higher periods of the S/N phase boundary, i.e., for $1<\Phi/\Phi_0<2$, etc. (Fig. 3). Taking into account the ''softness'' of the current loops in a real structure, which, strictly speaking, is not a one-dimensional network, the presence of disorder in these loops is quite probable. Therefore, one may assume that one of the reasons for the variation of the $T_c(\Phi/\Phi_0)$ peaks from period to period can be related to an areal disorder of ''soft'' current loops in the 2×2 antidot cluster.

Another important factor is the disorder arising from width inhomogeneity, structural defects, and nonidentical electrical properties of each wire, which can lead to a modification of the critical current of the individual wires and to a distribution of the effective area per cell. The importance of areal disorder was already stressed in studies of the phase boundary in wire networks[28,29] where it was shown that areal disorder can lead to a decay of the oscillation amplitudes and in some cases even to beatings in the envelope. Measurements on Josephson-junction clusters (JJC's) (Ref. 30) showed that coupling disorder coming from an unavoidable spread in junction parameters is not averaged out as in large arrays, leaving a clear trace in the transport properties.

Curve (c) in Fig. 8 shows the influence of areal disorder on the theoretical phase boundary of the antidot cluster. The areal disorder was introduced by allowing the coordinates of the nodes to vary randomly within a circle of radius 0.1 μm around the node position for the ordered network. In this way a random distribution of lengths l_{ij} and cell areas is generated that lifts the degeneracy of the possible states and changes the relative positions of the different parabolic energy branches. For small fields (i.e., the first period), the deviations with respect to curve (b) are not very pronounced, and it is still possible to identify all five parabola forming the $T_c(B)$ phase boundary. As the field increases, the oscillation amplitude gets smaller and the positions of the different branches shift, making the identification of the states less straightforward. From this analysis it is clear that disorder can indeed cause a shift of the peaks with increasing magnetic field, as it is observed experimentally. Finally, in curve (d) we have included the contributions of the parabolic background [curve (b)] and the areal disorder [curve (c)]. A comparison of curve (d) with the experimental data of Fig. 3 shows that certainly these two contributions are playing a role in our measurements. Nevertheless, even by including these two effects in the model, it is still not possible to simulate the experimental curves completely. This is probably due to the fact that we have used a one-dimensional approach, which cannot take into account the 2D character of the structure.

B. Critical currents and $V(I)$ characteristics

So far we have considered the effects of the vortex confinement by the 2×2 antidot cluster on the S/N phase boundary $T_c(B)$. In order to demonstrate that the unique properties of the Pb/Cu 2×2 antidot cluster are not restricted to the S/N phase transition, we present below the critical current results and the $V(I)$ characteristics measured at temperatures 400 mK$<T_c-T<$100 mK. We will show that at these temperatures the quantized states are still present and that the most stable ones at the S/N phase boundary do not always correspond to the states carrying the highest currents. In addition, we will demonstrate that a transport current $j\neq0$ is able to lift some of the degeneracies of the vortex configurations at $j=0$. The $V(I)$ characteristics will be used to give a qualitative picture of the flux-line transport in these nanostructures in terms of phase-slip processes.

It is known that the dynamics of 1D wires[31,32] and arrays of 1D wires[3] are mostly governed by phase-slip processes when currents close to the depairing critical current are sent through the wires. Thus, one may also expect that signatures of these processes should also be present in the $V(I)$ characteristics of the 2×2 antidot cluster. In such a phase-slip process, the energy of the system is reduced by bringing a small spot of the 1D wire [of the order of the quasiparticle diffusion length, $\lambda_Q^*\simeq\xi(T)$] momentarily to the normal state.

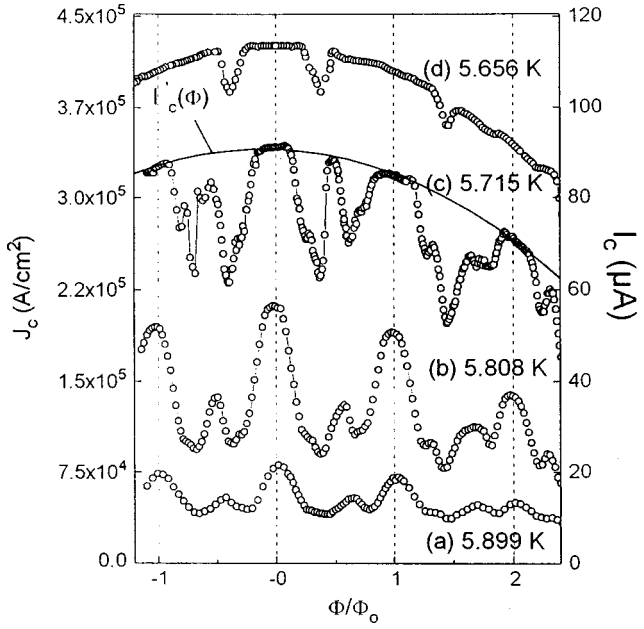

FIG. 9. Critical current density of the 2×2 antidot cluster as function of the reduced flux Φ/Φ_0 at four temperatures. (a) $T=5.899$ K, (b) $T=5.808$ K, (c) $T=5.715$ K, and (d) $T=5.656$ K.

During this process, the phase of the superconducting order parameter in that spot is changed by 2π. To preserve the superconductivity in the sample in the presence of a large current, the phase-slip process repeats in time and the average period τ between phase slips is related to the voltage measured between the two ends of the wire through the Josephson relation, $V=(\hbar/2e)2\pi/\tau$. The points where the order parameter becomes zero and its phase shows jumps of 2π, are known as phase-slip centers (PSC's). Obviously, if the wire already has some weak superconducting points, the PSC's will be localized at these spots.

Several mechanisms of PSC formation have been reported. First, PSC's can nucleate when the current exceeds the depairing critical current of the 1D wire, as described by the theory of Skocpol, Beasley, and Tinkham.[31] In this case, the formation of 1,2,...n PSC's gives rise to a steplike $V(I)$ characteristic.

PSC's can also be formed as a result of thermodynamic fluctuations that take place with a probability proportional to $\exp(-\delta\mathcal{F}/k_BT)$, where $\delta\mathcal{F}=w\sqrt{2}E_Jl/3\xi(T)$ is the free-energy barrier between the state before and after the phase slip. The theoretical description of PSC's was developed by Langer and Ambegoakar.[33] Taking into account the exponential decrease of the phase-slip probability with temperature, their model is only applicable in a very narrow temperature interval near T_c.

A third mechanism has recently been reported by Giroud *et al.*[3] for arrays of 1D wires with localized vortices. They consider the possibility that when a current close to the depairing critical current is reached in one of the wires, the vortex feels a ''Lorentz-like'' force perpendicular to the transport current, which tends to move the vortex to the next cell where the process is repeated. This model assumes the nucleation of a phase slip in a 1D wire each time that a vortex crosses the 1D wire.

1. Critical currents: Experimental results and comparison with the model

The critical current density versus magnetic field $J_c(B)$ of the 2×2 antidot cluster was determined with a criterium of 3 μV, as explained in Sec. II A. Then, at specific values of the magnetic field and temperature, the $V(I)$ characteristics were measured to confirm the $J_c(B)$ results and study the vortex dynamics in the antidot cluster.

Figure 9 shows the $J_c(B)$ curves measured at four temperatures. Note that clear maxima are observed at $n\Phi_0$ and $(n+0.5)\Phi_0$, and smaller inflections are detected around $(n+0.3)\Phi_0$ and $(n+0.7)\Phi_0$ [see Figs. 9(b) and 9(c)]. Initially, the magnitude of the oscillations increases by decreasing the temperature [Figs. 9(a) and 9(b)] but they disappear almost completely when further decreasing the temperature [see Fig. 9(d)]. A parabolic background caused by the magnetic-field penetration in the elementary wires is again observed at all temperatures.

The magnetic-field values at which specific features appear in $J_c(B)$ (Fig. 9) and $T_c(B)$ (Fig. 3) are the same. Thus one may assume that the maxima observed in the $J_c(B)$ of the 2×2 antidot cluster are related to certain stable vortex states revealed in the $T_c(B)$ oscillations. However, the relative amplitude of these maxima in one period of Φ_0 is different for $J_c(B)$ than for $T_c(B)$. In $T_c(B)$, large minima were observed at $n\Phi_0$, and three smaller minima of the same energy were obtained at around $(n+0.3)\Phi_0$, $(n+0.5)\Phi_0$, and $(n+0.7)\Phi_0$. On the contrary, in $J_c(B)$ the maxima at $n\Phi_0$ are followed in magnitude by the maxima at $(n+0.5)\Phi_0$, whereas the features appearing at $(n+0.3)\Phi_0$ and $(n+0.7)\Phi_0$ have almost completely lost their amplitude.

To estimate the field dependence of the critical current theoretically and compare it with the experimental observations, we have used the model described in Sec. III A 2 and solved Eqs. (3.5) and (3.6) for the case where the external transport current enters the structure at node (a) and leaves at the opposite side (see Fig. 5). The current-phase relation, given by Eq. (3.2), has slightly been modified to take into account the order-parameter depression in the strands when the current is close to the depairing current.[32] We have used the relation

$$I_{ij}=I_0\left(\frac{\gamma_{ij}}{\gamma_c}\right)\left[1-\frac{1}{3}\left(\frac{\gamma_{ij}}{\gamma_c}\right)^2\right], \tag{3.14}$$

which is linear for small phase differences and becomes parabolic near $\gamma_{ij}=\gamma_c$, where $\gamma_c\equiv l/(\sqrt{3}\xi)$ is the critical phase difference at which a phase-slip process occurs and $I_0\gamma_c=I_{dep}^{GL}$ is the Ginzburg-Landau depairing current. Note that Eq. (3.14) is identical to the current-phase relation obtained for a long ideal weak link in the depairing limit.[34]

The set of nonlinear equations for the unknown phase differences γ_{ij}, obtained from Eqs. (3.5) and (3.6), was solved numerically using the standard Newton-Raphson method.[35] The critical current at a magnetic flux Φ and a fixed state n_k $(k=1,...,4)$ was obtained as follows: First, the γ_{ij}'s were initialized to zero, I_a^{ext} was fixed at a certain value and the corresponding phases were determined. Next, the external current was slowly ramped up and the same procedure was repeated until the current was too high to find any

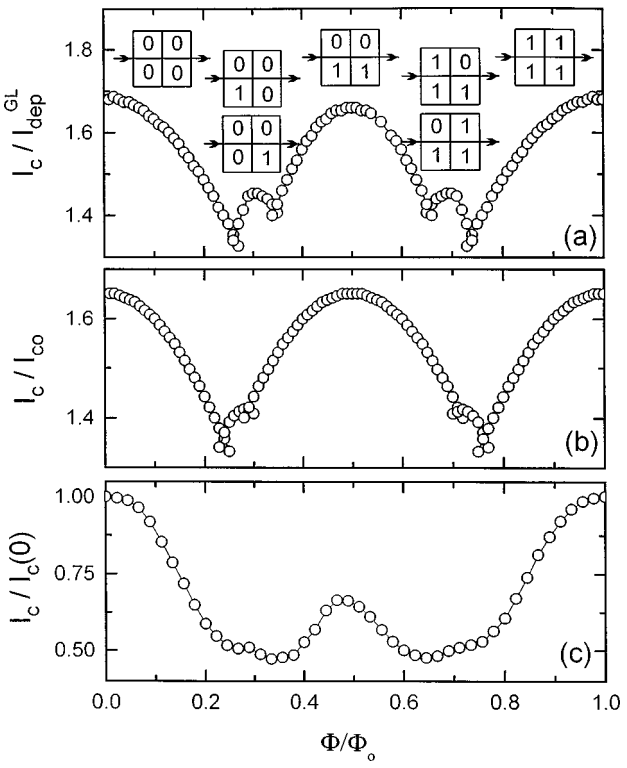

FIG. 10. Critical current versus the reduced flux per cell for (a) the current-phase relation given by Eq. (3.14) and (b) for a sinusoidal current-phase relation. The vortex states generated in the 2×2 antidot cluster at high transport currents are shown. (c) Experimental critical current versus reduced flux per cell at $T=5.808$ K with the background subtracted.

solution for the set of equations. The external current, above which no static solution exists, has been taken as the intrinsic critical current of the structure. The self-field induced by the transport current was estimated to be not higher than 0.1% and was therefore neglected in the analysis.

Curve (a) in Fig. 10 shows the theoretical $I_c(\Phi)$ obtained with Eq. (3.14) and $\gamma_c=\pi/2$. Only the states with the highest critical current at that particular Φ are shown, and we have restricted ourselves to the first period without considering any disorder. Because of the current injection at node (a), the symmetry is broken and the resulting vortex configurations differ from the ground-state configurations at zero applied current, discussed in Sec. III A 2.

The possible states are displayed schematically in Fig. 10(a). Only two states with one vortex in the structure are possible, instead of the fourfold degenerate ground state obtained for the case of $I_a^{ext}=0$. Near $\Phi=\frac{1}{2}\Phi_0$, the supercurrent is carried by a state where the vortices occupy the second row of the cluster (parallel state) instead of being located on the diagonals (checkerboard configuration).

The reason for the substantial modification of the stable vortex configurations is of course that the external current is added to the circular currents that flow to satisfy the fluxoid quantization. The total amount of current that can be injected before the structure depairs is higher if the transport and circular shielding currents are subtracted. For the case of large weakly coupled wire networks[5] and inductive JJA's (Ref. 36), it was already predicted that large transport currents make the checkerboard ground state unstable. This leads to a state of parallel vortex rows that can move coherently (driven vortex lattices) over the underlying periodic array.

Curve (b) in Fig. 10 shows the static calculation for a JJC having a sinusoidal current-phase relation for comparison. Besides some minor differences concerning the exact positions of minima and maxima [compare curves (a) and (b) in Fig. 10], the same states can be identified in the $I_c(\Phi)$ plot. Note, however, that in this case the normalizing current I_{c0} is the Josephson critical current and not the depairing current.

If in the case of the antidot cluster [curve (a)], $\gamma_c>\pi/2$, the overall shape of the calculated $I_c(\Phi)$ curve slightly changes and the difference with the JJC curve is more important, although the same states still carry the largest supercurrent. If we compare the theoretical curve (a) with the first period of the experimental data shown without the background for $T=5.808$ K in Fig. 10(c), we note that the curves are qualitatively similar. The same five states are clearly present. The state at $\Phi/\Phi_0=0.5$ has a higher I_c than the states around $\Phi/\Phi_0=0.3$ and 0.7, though it does not reach the same current value as predicted in the calculation, except for temperatures below approximately 5.715 K.

Below this temperature ($T=5.715$ K), the peaks at $n\Phi_0$ flatten and the amplitude of the modulations of the critical current decreases with decreasing temperature. It seems that the intrinsic $I_c(\Phi)$ behavior of the structure is cut off by a superimposed parabolic $I_c'(\Phi)$ background (see the full line in Fig. 9). The disappearance of the substructure with decreasing temperature was also observed in wire networks[5] and attributed to an increase of the energy barrier required to cross the superconducting wires.

In our case however, it looks more like a cutoff rather than a continuous decrease. Therefore, we believe that the effect could be caused by the propagation of heat generated in the current leads. Since the antidot structure can be considered as a kind of parallel circuit having a critical current that is a factor approximately 1.7 times higher than the depairing current (I_{dep}^{GL}) of a single wire [see Fig. 10(a)], the current lead is probably in a resistive state while the structure is still not. We measured the voltage between the nodes (a) and (b) (see Fig. 5), thus the voltages appearing over the current leads should not have influenced the results. However, at lower temperatures (when I_c is rather high), the actual heating due to this current cannot be excluded. If such heat propagates towards the antidot cluster, it could trigger a transition to a dissipative state earlier than expected. In that case, the $I_c(\Phi)$ dependence would show a ''cutoff'' governed by the parabolic critical current dependence of the current leads, $I_c'(\Phi)$.

Besides this influence of the current leads at high current levels, care should also be taken not to overestimate the limits of validity of the static simulation itself. Unlike the case of JJA's where the dynamics can relatively easy be taken into account by using the resistively shunted Josephson junction model in combination with the Josephson voltage relation,[37] it is not so straightforward to describe the dynamics in wire networks where resistive PSC's nucleate and can be activated throughout the structure. The present model does not take into account any dynamic effects such as vortex motion or propagating PSC's and, therefore, the critical

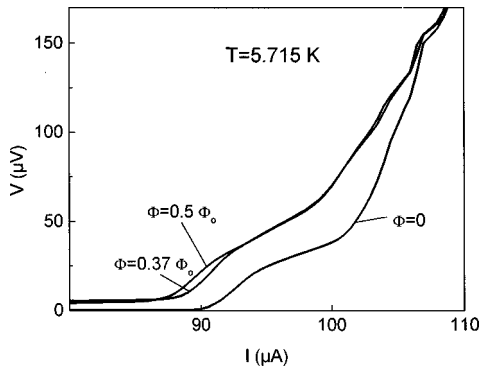

FIG. 11. $V(I)$ characteristics of the 2×2 antidot cluster measured at $T=5.715$ K for zero applied magnetic field and a magnetic field of 3 and 12 G. In all the curves similar characteristic steps can be distinguished.

currents obtained by the static simulation should be considered as an estimate of the upper limit rather than an accurate determination.

2. *V(I)* characteristics: Results and discussion

Figure 11 shows three $V(I)$ curves measured at $T=5.715$ K for three magnetic fields as representative data. Note that in all the curves, several steps are observed that depend on the applied magnetic field. However, an enlargement of the lower part of the $V(I)$ characteristics (see Fig. 12) shows that a quasilinear dissipative foot is clearly observed for the cases of $\Phi\neq n\Phi_0$. Note that this foot strongly depends on the magnetic field. In Fig. 12 we show three curves corresponding to $\Phi=\Phi_0$, $\Phi=0.37\Phi_0$, and $\Phi=0.5\Phi_0$ for $T=5.808$ K and $T=5.715$ K. Indicated by a horizontal dotted line is the 3 μV criterion used to determine the $I_c(\Phi)$ of Fig. 9.

When $\Phi=n\Phi_0$, no foot is observed at any temperature. Figure 13 shows the linear dependence of the critical current $I_c^{2/3}$ of the Pb/Cu 2×2 antidot cluster versus T/T_c for the measurements performed at zero magnetic field. I_c follows the $(1-T/T_c)^{3/2}$ dependence expected from the Ginzburg-Landau depairing critical current of 1D wires. The extrapolation of the $(1-T/T_c)^{3/2}$ law to $T/T_c=0$ results in $I_c(0)=7$ mA.

On the other hand, an estimation of the theoretical Ginzburg-Landau value for the depairing critical current of a 1D wire gives

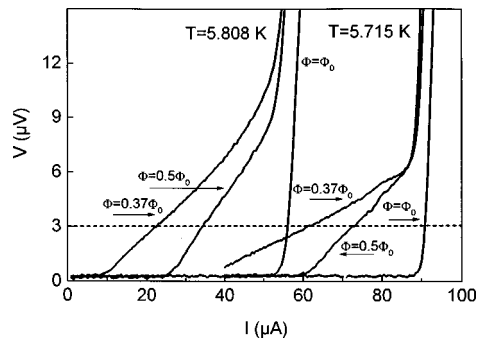

FIG. 12. Enlargement of the lower part of the $V(I)$ characteristics for a reduced flux $\Phi=\Phi_0$, $\Phi=0.37\Phi_0$, and $\Phi=0.5\Phi_0$ at $T=5.808$ K and $T=5.715$ K.

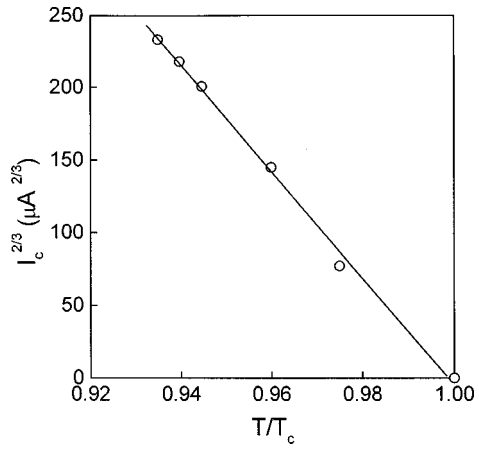

FIG. 13. Temperature dependence of the critical current measured at $B=0$ showing the same behavior as the depairing critical current of 1D wires.

$$I_{dep}^{GL}(0)=\frac{\Phi_0 wd}{3\sqrt{3}\pi\mu_0\lambda(0)^2\xi(0)}, \tag{3.15}$$

where w and d are the width and thickness of the wires, respectively, and $\xi(0)$ and $\lambda(0)$ were determined in Sec. II B. As shown in the previous section [see Fig. 9(a)], the depairing current of the structure is $I_c^{th}(0)\approx1.6I_{dep}^{GL}(0)=72$ mA, which is one order of magnitude higher than the experimental value obtained. It should, however, be noted that we have underestimated the value of $\lambda(0)$ by equating it to that of the single Pb layer $\lambda_{Pb}(0)$, while, in fact, we should use $\lambda_{NS}>\lambda_{Pb}$ (see Sec. II B). From the above analysis, we can estimate an effective penetration depth for the Pb/Cu bilayer $\lambda_{NS}(0)\approx3\lambda_{Pb}(0)$.

When $\Phi\neq\Phi_0$, we believe that the field-dependent linear foot that appears at low currents in the $V(I)$ characteristics is induced by phase-slip processes. More precisely, by the mechanism reported by Giroud *et al.*[3] for arrays of 1D wires that claims that vortices may move from one cell to the other in a direction perpendicular to the transport current in a kind of stationary ''flux-flow'' regime. In this model a vortex jump from one antidot to another should lead to a phase slip induced in the 1D wire crossed by the vortex. Dissipation in arrays due to the vortex motion has also been reported by other authors.[4,5] This mechanism may explain the disappearance of the resistive foot at $\Phi=n\Phi_0$. Since we have shown that at $\Phi=n\Phi_0$ an edge surface current is flowing in the antidot cluster, no vortices are present inside the antidot cluster. Thus, if the dissipative foot is induced by the motion of vortices, no foot should be expected at $\Phi=n\Phi_0$.

The possibility of vortex motion was not considered for the critical current calculation in the previous section. There we determined the critical current of the structure using a static approach, i.e., the I_c was defined as the maximum I that could keep zero voltage through the structure and still fulfill the fluxoid quantization condition and current conservation equations. The real critical current values may therefore be lower than the ones obtained by means of the static approach. The experimental evidence supporting the idea that motion of vortices in the antidot cluster induces phase-slip processes and thus gives rise to dissipation at $I<I_c$, is presented below.

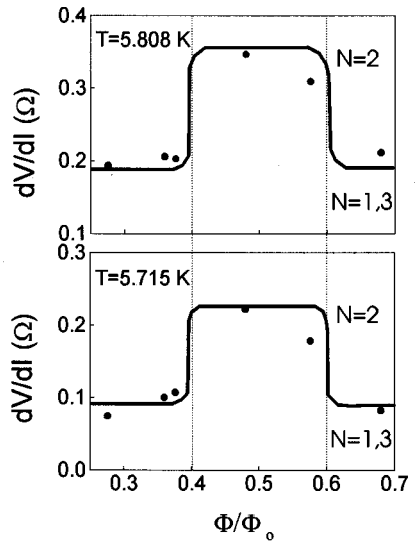

FIG. 14. Differential resistance determined at the onset of the dissipative foot of the $V(I)$ characteristics as a function of the reduced flux for $T=5.808$ K and $T=5.715$ K. The solid line is a guide for the eyes showing the two levels expected from the model of vortex motion induced by phase slips. The dotted lines indicate the Φ/Φ_0 values at which a change of vortex configuration is observed experimentally.

Figure 14 shows the differential resistance, dV/dI, as a function of the reduced flux Φ/Φ_0, determined at the onset of the dissipative foot in the $V(I)$ characteristic for $T=5.808$ K and $T=5.715$ K (Fig. 12). Since the $V(I)$ characteristic for the dissipative foot is quasilinear, we have extracted one single value for the differential resistance at each Φ/Φ_0. Figure 14 shows the dV/dI for the Φ/Φ_0 interval where the current is flowing in the internal strands of the 2×2 antidot cluster. The interval where only an edge surface current is flowing in the antidot cluster has been omitted since, there, no foot is observed. We have denoted by vertical dashed lines the Φ/Φ_0 values at which a change of vortex configuration was experimentally observed. Note that, at both temperatures, the dV/dI can be defined by two levels: a low level that accounts for the one-vortex configuration ($N=1$) and three-vortex configuration ($N=3$) or also called one-antivortex configuration, and a high level given by the two-vortex configuration ($N=2$). This two level representation strongly suggests that the dissipative foot might be caused by a ''flux-flow'' motion of vortices as reported also by Giroud *et al.*[3] for wire networks. In this model, a vortex crossing one cell is associated to a 2π phase jump, which generates a voltage in a time τ given by the Josephson relation

$$V=\frac{\hbar}{2e}\frac{2\pi}{\tau}. \tag{3.16}$$

If we assume that the stationary dissipation process can be described by a constant average vortex velocity v [as in the case of classical flux-flow in type-II superconductors[38] and JJA's (Ref. 39)], the voltage generated by the net motion of N vortices can be written as

$$V=\frac{\hbar}{2e}\frac{2\pi}{\tau}f=N\Phi_0\frac{v}{a}. \tag{3.17}$$

On the other hand, since this model associates a PSC to each vortex jump, we have equated the total average power $V[I-I_c(\Phi)]$ generated in the cluster to the sum of powers dissipated by each individual PSC, $P_{PSC's}=Ni_Q^2R_n2\lambda_Q^*/a$, where here N is the number of PSC's, i_Q is the quasiparticle current flowing in each wire, R_n is the normal-state resistance of a single wire and λ_Q^* is the quasiparticle diffusion length. From this equality, and assuming that $i_Q\simeq(I-I_c)/3$,[3,31] we have determined an average vortex velocity

$$v\approx\frac{R_n2\lambda_Q^*(I-I_c)}{9\Phi_0}, \tag{3.18}$$

which is proportional to the current $(I-I_c)$. By substituting this velocity in Eq. (3.17) and calculating the differential resistance at the critical current (I_c), we obtain

$$\left(\frac{dV}{dI}\right)_{I_c}=\frac{2}{9}\frac{NR_n\lambda_Q^*}{a}. \tag{3.19}$$

From Eq. (3.19), and taking $\lambda_Q^*\simeq\xi(T)$ and $N=1$ for the one-vortex configuration and $N=2$ for the two-vortex configuration, we have determined the following differential resistances: At $T=5.715$ K, $dV/dI\simeq0.1\,\Omega$ for $N=1$ and $dV/dI\simeq0.2\,\Omega$ for $N=2$, which is in good agreement with the values given in Fig. 14. At $T=5.808$ K, $dV/dI\simeq0.12\,\Omega$ for $N=1$ and $dV/dI\simeq0.24\,\Omega$ for $N=2$. In this case, the values shown in Fig. 14 are higher, although their ratio still remains approximately correct. These calculations also point in the direction that the dissipative foot can be interpreted in terms of vortex motion.

At higher currents, the $V(I)$ characteristics do not show a continuous increase of voltage with increasing current but instead they are composed of several voltage steps (see Fig. 11). The transition to the normal state of a 1D wire is produced by the generation of steady PSC's that increase in number as the transport current grows. This dissipation phenomenon correlates the differential resistance with the number of PSC's created in the wire and therefore results in a $V(I)$ curve with characteristic steps. Although the steps observed in the $V(I)$ curve in Fig. 11 are not steep like the ones reported for single 1D wires[31] and infinite wire networks[3] interpreted by the SBT theory, we believe that they are reminiscent of the resistive transition of the quasi-one-dimensional wires constituting the antidot cluster. A nonstrictly 1D character of the wires forming the antidot cluster may be one of the reasons for the smoothness of the steps.

IV. CONCLUSIONS

We have studied the transport properties of a Pb/Cu 2×2 antidot cluster (a microsquare with four antidots) by measuring the superconducting/normal phase boundary, critical currents, and $V(I)$ characteristics. The Pb/Cu bilayer can be considered as a single superconducting entity with superconducting parameters that are somewhat different than those of the single Pb layer. The presence of the antidots leads to a characteristic structure in the magnetoresis-

tance and phase boundary caused by the formation of well-defined vortex configurations. By comparison of the experimental results with calculations that approximate the cluster as a 1D micronetwork, we were able to identify the corresponding ground states.

The formation of particular vortex states, as the magnetic field is varied, was also observed in the critical current versus field curves. Comparison with a static model showed that the current injection lifts the degeneracy and that the vortex states at larger current differ from the ground states, observed in the phase boundary $T_c(B)$.

The dissipative processes were probed for the different vortex occupations by means of $V(I)$ measurements. We find clear evidence for a stationary vortex motion at the onset of dissipation and the creation of phase-slip centers at larger voltages and currents.

ACKNOWLEDGMENTS

We thank M. Kuprianov, A. López, H. Fink, A. Buzdin, M. Baert, J. G. Rodrigo, and V. Bruyndoncx for helpful discussions. This work was supported by the Belgian Inter-University Attraction Poles (IUAP), the Flemish Concerted Action (GOA), VIS, and the National Fund for Scientific Research (FWO-Vlaanderen) programs. One of us (T.P.) thanks the European Training and Mobility of Researchers Program for financial support.

*Present address: Institut de Ciencia de Materials de Barcelona (CSIC), Campus UAB, 08193 Bellaterra, Spain.

[1] *Proceedings of the Nato Workshop on Coherence in Superconducting Networks*, edited by J. E. Mooij and G. B. J. Schön [Physica B **152** (1988)]; *Proceedings of the ICTP Workshop on Josephson Junction Arrays*, edited by H. A. Cerdeira and S. R. Shenoy [Physica B **222** (1996)].

[2] B. Pannetier, in *Quantum Coherence in Mesoscopic Systems*, edited by B. Kramer (Plenum, New York, 1991).

[3] M. Giroud, O. Buisson, Y. Y. Wang, B. Pannetier, and D. Mailly, J. Low Temp. Phys. **87**, 683 (1992).

[4] H. S. J. van der Zant, M. N. Webster, J. Romijn, and J. E. Mooij, Phys. Rev. B **42**, 2647 (1994).

[5] H. S. J. van der Zant, M. N. Webster, J. Romijn, and J. E. Mooij, Phys. Rev. B **50**, 340 (1994).

[6] M. Baert, V. V. Metlushko, R. Jonckheere, V. V. Moshchalkov, and Y. Bruynseraede, Phys. Rev. Lett. **74**, 3269 (1995).

[7] M. Bezryadin and B. Pannetier, J. Low Temp. Phys. **98**, 251 (1995).

[8] E. Rosseel, V. V. Metlushko, M. J. Van Bael, M. Baert, T. Puig, K. Temst, V. V. Moshchalkov, and Y. Bruynseraede, Czech. J. Phys. **46**, 885 (1996).

[9] V. V. Moshchalkov, M. Baert, V. V. Metlushko, E. Rosseel, M. J. Van Bael, K. Temst, R. Jonckheere, and Y. Bruynseraede, Phys. Rev. B **54**, 7385 (1996).

[10] E. Rosseel, M. J. Van Bael, M. Baert, R. Jonckheere, V. V. Moshchalkov, and Y. Bruynseraede, Phys. Rev. B **53**, R2983 (1996).

[11] T. Puig, E. Rosseel, M. Baert, M. J. Van Bael, V. V. Moshchalkov, and Y. Bruynseraede, Appl. Phys. Lett. **70**, 3155 (1997).

[12] P. G. de Gennes, C. R. Seances Acad. Sci., Ser. 2 **292**, 279 (1981); S. Alexander, Phys. Rev. B **27**, 1541 (1983).

[13] D. Neerinck, K. Temst, H. Vanderstraeten, C. Van Haesendonck, Y. Bruynseraede, A. Gilabert, and I. K. Schuller, in *Layered Structures: Heteroepitaxy, Superlattices, Strain, and Metastability*, edited by B. W. Dodson, L. J. Schowalter, J. E. Cunningham, and F. H. Pollak, MRS Symposia Proceedings No. 160 (Materials Research Society, Pittsburgh, 1990). p. 599.

[14] G. T. Meaden, *Electrical Resistance of Metals* (Plenum, New York, 1965), p. 4.

[15] D. Neerinck, Ph.D. thesis, Katholieke Universiteit Leuven, 1991.

[16] K. R. Biagi, V. G. Kogan, and J. R. Clem, Phys. Rev. B **32**, 7165 (1985).

[17] P. G. de Gennes, *Superconductivity of Metals and Alloys* (Addison-Wesley, Reading, MA, 1966).

[18] P. G. de Gennes, Rev. Mod. Phys. **36**, 225 (1964).

[19] A. Gilabert, Ann. Phys. (Paris) **2**, 203 (1977).

[20] M. Tinkham, *Introduction to Superconductivity* (McGraw-Hill, New York, 1975).

[21] V. V. Moshchalkov, L. Gielen, C. Strunk, R. Jonckheere, X. Qiu, C. Van Haesendonck, and Y. Bruynseraede, Nature (London) **373**, 319 (1995).

[22] R. Benoist and W. Zwerger, Z. Phys. B **103**, 377 (1997).

[23] C. C. Chi, P. Santhanam, S. J. Wind, M. J. Brady, and J. J. Bucchignano, Phys. Rev. B **50**, 3487 (1994).

[24] C. C. Chi and P. Santhanam, J. Low Temp. Phys. **88**, 163 (1992).

[25] V. V. Moshchalkov, L. Gielen, M. Baert, V. Metlushko, G. Neultiens, C. Strunk, V. Bruyndoncx, X. Qiu, M. Dhallé, K. Temst, C. Potter, R. Jonckheere, L. Stockman, M. J. Van Bael, C. Van Haesendonck, and Y. Bruynseraede, Phys. Scr. **T55**, 168 (1994).

[26] H. J. Fink and S. B. Haley, Phys. Rev. Lett. **66**, 216 (1991).

[27] H. J. Fink, O. Buisson, and B. Pannetier, Phys. Rev. B **43**, 10 144 (1991).

[28] M. A. Itzler, A. M. Behrooz, C. W. Wilks, R. Bojko, and P. M. Chaikin, Phys. Rev. B **42**, 8319 (1990).

[29] S. P. Benz, M. G. Forrester, M. Tinkham, and C. J. Lobb, Phys. Rev. B **38**, R2869 (1988).

[30] S. V. Rao and D. J. Van Harlingen, Phys. Rev. B **48**, 12 853 (1993).

[31] W. J. Skocpol, M. R. Beasley, and M. Tinkham, J. Low Temp. Phys. **16**, 145 (1974).

[32] B. I. Ivlev and N. B. Kopnin, Adv. Phys. **33**, 47 (1984).

[33] J. S. Langer and V. Ambegoakar, Phys. Rev. **164**, 498 (1967).

[34] K. K. Likharev, Rev. Mod. Phys. **51**, 101 (1979).

[35] W. H. Press, B. P. Flannery, S. A. Teukolsky, and W. T. Vetterling, *Numerical Recipes in Pascal* (Cambridge University Press, Cambridge, 1990).

[36] J. R. Phillips, H. S. J. van der Zant, and T. P. Orlando, Phys. Rev. B **50**, 9380 (1994).

[37] J. S. Chung, K. H. Lee, and D. Stroud, Phys. Rev. B **40**, 6570 (1989).

[38] J. Bardeen and M. J. Stephen, Phys. Rev. A **140**, A1197 (1965).

[39] T. P. Orlando, J. E. Mooij, and H. S. J. van der Zant, Phys. Rev. B **43**, 10 218 (1991).